ACS ES&T Engineering

pubs.acs.org/estengg

Article

Mechanism of a Mussel-Inspired Polydopamine-Modified Bioaffinity Spider Silk Self-Cleaning Photocatalyst for Enhanced Bioaerosol Purification

Linghui Peng, Weina Zhao, Fukai Xu, Manlin Dong, Guiying Li, Weiping Zhang, Zhishu Liang, Taicheng An,* and Huijun Zhao

Cite This: https://doi.org/10.1021/acsestengg.6c00164

Read Online

ACCESS | Metrics & More | Article Recommendations | Supporting Information

ABSTRACT: The demand for self-cleaning air purification is urgently increasing due to concerns for human health and long-term use. Herein, this study investigated the enhanced mechanism of a self-cleaning artificial spider silk (PMAS) photocatalyst, which was modified by bioaffinity polydopamine (PDA) for highly efficient bioaerosol adhesive capture and photocatalytic inactivation. By increasing the bioaffinity of the PMAS photocatalyst, bioaerosols can adhere to the surface, increasing capture efficiency by 50−700%. The captured bioaerosols were concentrated on the spindle knots of the PMAS photocatalyst, forming droplet reactors for subsequent photocatalytic inactivation. Through a combination of experiments and calculations, the mechanism of enhanced capture efficiency by the PMAS photocatalyst was revealed: PDA endows doubled adsorption energy and tripled adhesion forces between the interfaces of bioaerosols and the photocatalyst due to the abundant indole and amino groups. PDA also provides hydrophilic properties to the PMAS photocatalyst, leading to a sevenfold increase in captured bacterial droplet volumes. Due to its bioaffinity, hydrophilic, and photocatalytic properties, the PMAS photocatalyst possesses self-cleaning capability by *in situ* inactivation of microorganisms and purification of self-washed debris, facilitating repeated use for long-term capture and regeneration of occupied active sites. This work may offer rational designs for a new generation of self-cleaning photocatalysts for air purification.

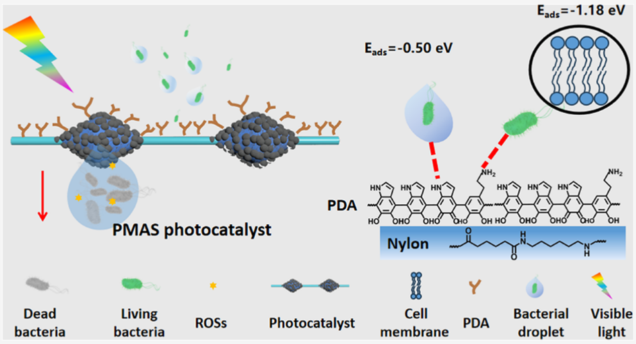

KEYWORDS: *bioaerosol purification, artificial spider silk photocatalyst, polydopamine surface modification, bioaffinity capture mechanism, self-cleaning principle*

1. INTRODUCTION

Airborne microorganisms are transmitted through small aerosolized particles that are suspended in the air (bioaerosols), which are responsible for spreading many serious infectious diseases in humans and animals.[1−5] Bioaerosols emitted from oceans, lakes, hospitals, landfills, and so on contain or absorb a lot of moisture and water droplets,[6−9] which may offer a breeding ground for the survival of microorganisms. Thus, air purification and bioaerosol control under humid conditions are urgent and crucial.[10] One of the most commonly used bioaerosol control strategies is air filtration, which works by intercepting, diffusing, and electrostatically attracting microorganisms onto porous and fibrous materials.[11−15] However, under high humidity conditions, the charge on the surface of the filter escapes quickly, resulting in a significant reduction in filtration efficiency. Therefore, the reduced efficiency, blockage, microorganism accumulation, and secondary contamination limit the long-term usage of these air filters for bioaerosol purification under high humidity conditions.[16−18]

Some technologies have been combined with filters to avoid microorganism accumulation and secondary contamination, including the linkage of metal ions, photocatalysts, and organic antibacterial agent[19−21] As an environmentally friendly and energy-saving technology, the photocatalytic strategy can be utilized in the control of bioaerosols, effectively inactivating them to prevent microbial proliferation and secondary contamination.[22] Liu et al. developed an rGO-TiO_2 composite photocatalyst on surface-etched plastic optical fibers for distributed UV transmission, achieving 100% *S. aureus* and *E.*

Received: February 20, 2026
Revised: March 20, 2026
Accepted: March 23, 2026

coli aerosol filtration and more than 98.15% inactivation efficiency.[23] Wang et al. immobilized a monolayer $Ti_3C_2T_x$ photocatalyst on a photocatalytic flow bed reactor, resulting in a 4 log inactivation efficiency of bioaerosols with only 14 s of residence time.[24] An et al. developed an artificial spider silk photocatalyst with periodic spindle knots to capture and concentrate bacterial microdroplets in the air and to inactivate 99.99% of bacteria *in situ*.[25] Recently, Warsinger et al. investigated photocatalytic technology to reduce the concentration of bioaerosols in air conditioning systems, showing that only captured microorganisms can be inactivated, and these flow bed photocatalytic systems cannot effectively capture bioaerosols with small sizes (1−5 μm).[26] Therefore, even though photocatalytic technology shows great potential for bioaerosol inactivation, the bioaerosol capture efficiency of the photocatalyst is a prerequisite for effective inactivation, facilitating interaction between the photocatalyst and microorganisms.

In high-humidity environments, bioaerosols exist in the form of airborne microorganisms and microbial droplets with low concentrations.[27−29] Therefore, the high bioaffinity and microorganism enrichment of photocatalysts for bioaerosol purification are urgently required. Inspired by the bioaffinity adhesion of mussels to various materials, dopamine has been identified as a candidate to provide strong adhesive forces to wet surfaces. This versatile dopamine can be used in various fields for forming polydopamine (PDA) thin films due to its bioaffinity, multifunctional groups,[30−35] self-assembly, and self-polymerization properties.[36−40] As PDA shows bioaffinity to biomolecules like proteins, nucleotides, oligosaccharides, and lipid assemblies,[40] it has been frequently applied to modify the surface of nanoparticles to improve the nondestructive capture of tumor cells[41] and to encapsulate drugs for targeting bacterial infections.[42] In addition, the functional groups in PDA are hydrophilic, which are also beneficial for capturing microdroplets in bioaerosols.[43] Therefore, PDA surface modification is an ideal candidate to improve the microorganism and bacterial droplet collection capability of photocatalysts, realizing highly efficient bioaerosol capture ability.[44−46]

By combining mussel-inspired bioaffinity PDA surface modification with the artificial spider silk photocatalyst (namely PMAS photocatalyst), PDA can offer high bioaffinity to airborne microorganisms under high humidity conditions to coordinate with the artificial spider silk basement, which provides the concentration and photocatalytic inactivation functions for the modified photocatalyst. Thus, PDA modification may also help realize the initial bioaffinity bioaerosol capture and subsequent purification of the PMAS photocatalyst in practical application systems. However, the interfacial interaction mechanisms of airborne microorganisms with the bioaffinity surface of the PMAS photocatalyst remain unrevealed; thus clarifying the underlying mechanisms of the bioaffinity capture process of the PMAS photocatalyst will also facilitate the capture and purification efficiency of bioaerosols. Thus, in this study, the PMAS photocatalyst was first developed, and the enhanced bioaffinity capture mechanisms, including the bonding modes of microorganisms/bacterial droplets to PDA on the photocatalyst, were elucidated through experimental validation with various surface analyses as well as density functional theory (DFT) simulations. In addition, the self-cleaning mechanism of this PMAS photocatalyst, based on photocatalytic inactivation and self-washing under high humidity conditions, was also investigated in detail. This PMAS photocatalyst may offer excellent bioaffinity capture and self-cleaning capabilities for long-term bioaerosol purification.

2. EXPERIMENTAL SECTION

2.1. Materials

Nylon fibers with a 60 μm diameter were obtained from Dongguan Deyongjia Textile Co., Ltd. Poly(methyl methacrylate) (PMMA) and titanium dioxide (P25) were obtained from Macklin Co., Ltd. Dopamine hydrochloride (98.5%), Tris-HCl (99.9%), N,N-dimethylformamide (DMF, 99.8%), ethanol, acetone, glutaraldehyde (50%), nutrient broth, and nutrient agar were purchased from Aladdin Co., Ltd.

2.2. Preparation of the PMAS Photocatalyst

The PMAS photocatalyst was prepared by a two-step dip-coating method, as demonstrated in our recent study, with some improvements.[25] Details are illustrated in Figure S1. Briefly, the nylon fiber was first immersed in a PMMA/(DMF+ethanol) suspension (10:100:1 by weight) and withdrawn quickly. After drying at room temperature, the pure artificial spider silk was subsequently immersed in TiO_2/PMMA/(DMF + ethanol) suspension (3:3:100:1 by weight) and quickly withdrawn. Then, the PMAS photocatalyst was placed into a dopamine hydrochloride solution for 24 h (0.2−1.0 g/L and pH = 8.5). The optical images of the PMAS photocatalyst at different steps are shown in Figure S2.

2.3. Material Characterization

The characterization details, including Raman spectroscopy, Electron Paramagnetic Resonance (EPR), Scanning Electron Microscopy (SEM), Atomic Force Microscopy (AFM), the aerodynamic diameter of the bioaerosols, X-ray Photoelectron Spectroscopy, and water contact angle, are described in Text S1.

2.4. Measurement of Bioaffinity Capture Performance of the PMAS Photocatalyst

Gram-negative *E. coli* (RK2) was used as a model bacterium in the bioaerosols for better observation. The plasmid of the *E. coli* bacteria contains a green fluorescent protein (GFP) marker gene, and the nucleoid contains a tomato-red marker gene, allowing alive/dead bacteria to be observed directly via fluorescent microscopy. All disks and materials were sterilized in an autoclave before the experiments. The bacterial cells were cultivated in nutrient broth for 12 h at 37 °C to yield a cell count of about 10^9 colony-forming units (CFU)/mL. Then, the bacterial cells were collected by centrifugation (8000 rpm for 2 min) and resuspended in sterile saline solution (0.9% w/v). Typically, 50 mL of bacterial suspension (10^3−10^9 CFU/mL) was poured into a glass bottle of the Collison bioaerosol generator. Clean air at 12.5 L/min was injected into the generator, and sprayed bioaerosols with an aerodynamic diameter of ∼1.2 μm (Figure S3) passed through the diffusion drying tube to control their relative humidity. The bulk PMAS photocatalysts (four 5 cm arrays) were placed in the flow of bioaerosols for 2 min to capture airborne bacteria and bacterial microdroplets. A detailed experimental setup is illustrated in Figure S4.

2.5. Evaluation of Self-Cleaning Performance of the PMAS Photocatalyst for Repeated Uses

The self-cleaning performance was also assessed by *in situ* microbial inactivation efficiency and self-washing properties. First, the *E. coli* bioaerosols were captured by the PMAS photocatalyst and then placed under visible light (xenon lamp, 100 mW/cm^2) for 0−4 h. To control the relative humidity, a humidifier and a diffusion dryer were applied to the system. After irradiation, the droplets concentrated onto the PMAS photocatalyst were collected, and the PMAS photocatalyst was washed with 20 mL saline solution in an ultrasonic bath for 10 min. The suspension was vortexed for 1 min and then diluted for plating. The number of colonies was enumerated through visual inspection after 18 h of cultivation. The bacterial inactivation efficiency was calculated. The self-washing property was characterized by SEM inspection after collecting microdroplets on the PMAS

https://doi.org/10.1021/acsestengg.6c00164
ACS EST Engg. XXXX, XXX, XXX−XXX

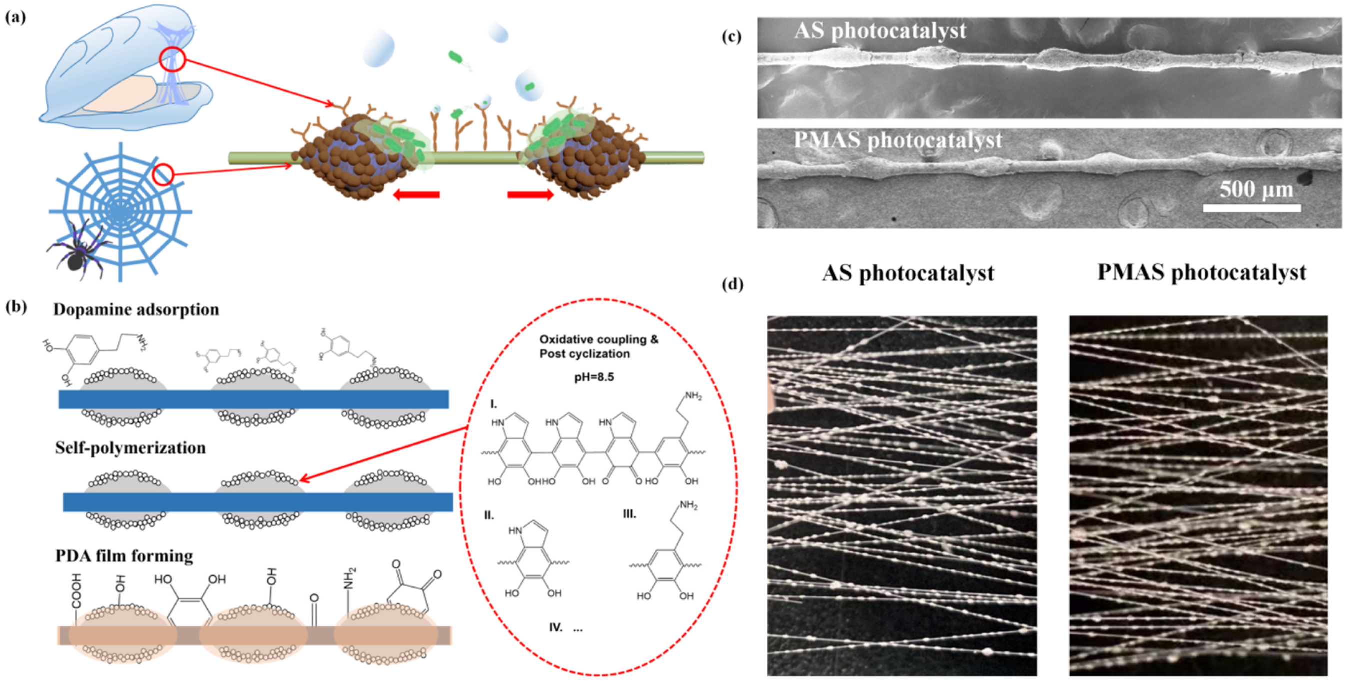

Figure 1. Illustration and characterization of PMAS photocatalyst. (a) Illustration of combining mussel surface adhesion with the shape of spider silk to form the PMAS photocatalyst; (b) Procedure for polydopamine modification of the PMAS photocatalyst; (c) SEM images and (d) optical images of PMAS and AS photocatalysts.

photocatalyst. The capture and self-washing experiments were repeated several times.

2.6. Density Functional Theory Calculations of Interaction Energy between Microorganisms and Water onto PDA

The density functional theory (DFT) calculations were performed using the DMol3 module in Materials Studio. The core electrons were treated using the all-electron method, and a double numerical plus polarization (DNP) basis set was applied with an orbital cutoff energy of approximately 400 eV. The convergence criteria were set as follows: an energy tolerance of 1×10^{-5} Hartree (1 Hartree = 27.21 eV), a maximum force of 0.004 Hartree/Å, and a maximum displacement of 0.005 Å. A smearing parameter of 0.005 Ha was used to facilitate structural convergence. A slab model of titanium dioxide with a vacuum layer of ∼15 Å was constructed to minimize periodic interactions. Details are illustrated in Text S2.

3. RESULTS AND DISCUSSIONS

3.1. Bioaerosol Capture Performance of the PMAS Photocatalyst

To clarify the capture performance of the PMAS photocatalyst, it was first prepared by combining the structure of spider silk with the surface modification strategy of mussels' mucus (Figure 1a) and characterized by SEM. As demonstrated in Figure 1b, the structure of PDA is complex, with various components, including type I, which consists of indole rings and amine groups, type II, which consists of indole rings, and type III, which consists of amine groups, and so on.[34,44,45] SEM images clearly showed the appearance of PMAS photocatalysts, possessing relatively uniform periodic spindle knots (Figure 1c), and the surface of the spindle knots is TiO_2 nanoparticles settled onto the PMMA, yielding TiO_2 nanoparticles that are highly exposed to the outside and anchored onto PMMA rather than embedded in PMMA (Figures S5−S8). From the SEM images, not much difference can be seen between the photocatalysts with and without PDA modification (AS photocatalysts). However, the color of the PMAS photocatalyst changed from white to brown after PDA surface modifications (Figure 1d). XPS analysis and UV−vis spectrum were also conducted to reveal the chemical components of the PMAS photocatalyst (Figure S9), confirming PDA formation on the surface of the PMAS photocatalyst and indicating that the PDA modification significantly enhances visible light absorption while retaining UV light absorption. In summary, the PMAS photocatalyst was successfully prepared for subsequent characterization.

To quantify the bioaerosol capture performance of the PMAS photocatalyst, the bioaerosol capture efficiency at different relative humidities (RHs), concentrations, and flow rates of bioaerosols was measured by counting the cultured colonies washed from it. As shown in Figure 2a, the number of bacteria captured onto the PMAS photocatalyst increased with the rise in RH. The number of captured bacteria at RH 99% is around 3 times that at RH 45%, indicating that high RH is conducive to enhancing the bioaerosol capture performance of this system. Specifically, the number of bacteria captured by the PMAS photocatalyst is also much higher (1.5 times at RH 99%) than that of the AS photocatalyst under identical conditions. For different concentrations of bioaerosols, the number of bacteria captured onto the PMAS photocatalyst increased from 10^4 to 10^6 CFU per 5 cm when the concentration of bacteria was increased, due to more bacteria interacting with the PMAS photocatalyst (Figure 2b). The PMAS photocatalyst can capture 7 times (10^3 CFU/mL) to 1.5 times (10^9 CFU/mL) more bacteria compared to the AS photocatalyst, increasing capture efficiency by 50−700%, and demonstrating the superiority of the PMAS photocatalyst in capturing bioaerosols at different concentrations, especially at low concentrations. This feature provides the PMAS photocatalyst with the opportunity to capture bioaerosols in actual atmospheric environments with high humidity, even when the

https://doi.org/10.1021/acsestengg.6c00164

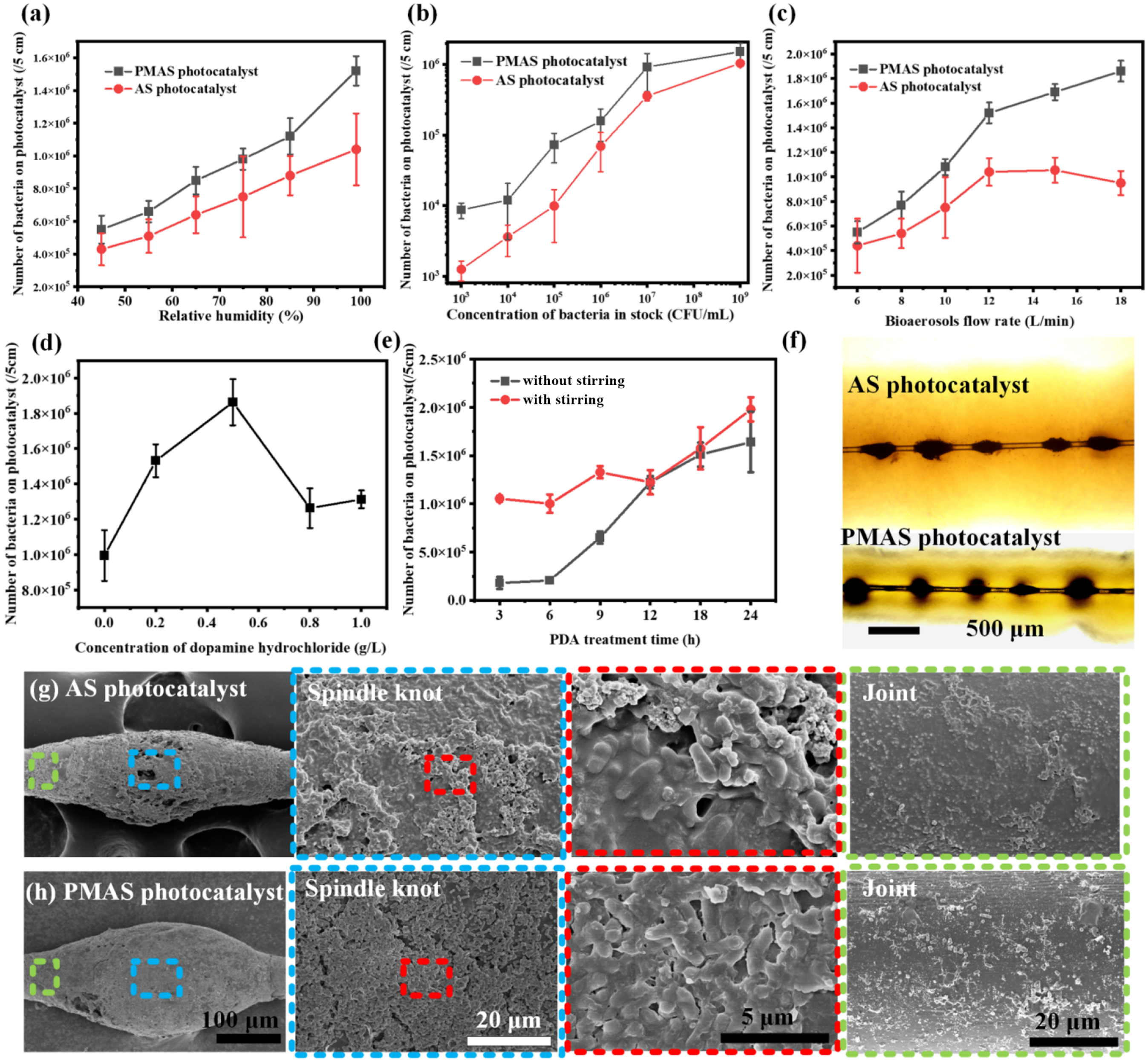

Figure 2. Bioaffinity capture performance of PMAS photocatalyst. Bioaerosol capture performance of PMAS and AS photocatalysts at different (a) humidity levels, (b) concentrations of bacteria, and (c) bioaerosol flow rates The influences of (d) concentration of dopamine hydrochloride and (e) PDA treatment time on the bioaerosol capture performance of the PMAS photocatalyst. Optical images of bacterial colonies grown along with (f) AS and PMAS photocatalysts after capturing. SEM images of captured bacteria on the spindle knots and joints of (g) AS and (h) PMAS photocatalysts.

concentration of atmospheric bioaerosols is relatively low (10^2–10^4 CFU/m^3). We also investigated the capture performance of the PMAS photocatalyst at different flow rates of bioaerosols (Figure 2c). Significantly, the number of captured bacteria increased with the rise in flow rate, as more bacteria passed through the PMAS photocatalyst at the same time. At a low flow rate (3 L/min), the number of bacteria captured by the PMAS photocatalyst is ~5×10^5 CFU per 5 cm. While at a high flow rate (18 L/min), the number of bacteria captured by the PMAS photocatalyst reached 1.8×10^6 CFU per 5 cm. It can be seen that the PMAS photocatalyst enhanced the capture performance by approximately two times at high bioaerosol flow rates compared to the AS photocatalyst, overcoming the problem of efficiency decrease observed in the AS photocatalyst at high flow rates These results indicate that the PDA modification of the PMAS photocatalyst can significantly improve bioaerosol capture performance under different environmental conditions, enabling better application in future practical environments.

Influences of different concentrations of dopamine hydrochloride (precursor of PDA) and treatment time of PDA on bioaerosol capture performance were also investigated to reveal how PDA modification procedures enhance the performance of the PMAS photocatalyst. From Figure 2d, the bioaerosol capture performance of the PMAS photocatalyst initially increased and then decreased with increasing concentrations of dopamine hydrochloride, reaching its peak at 0.5 g/L. According to SEM images of the PMAS photocatalyst with

https://doi.org/10.1021/acsestengg.6c00164
ACS EST Engg. XXXX, XXX, XXX−XXX

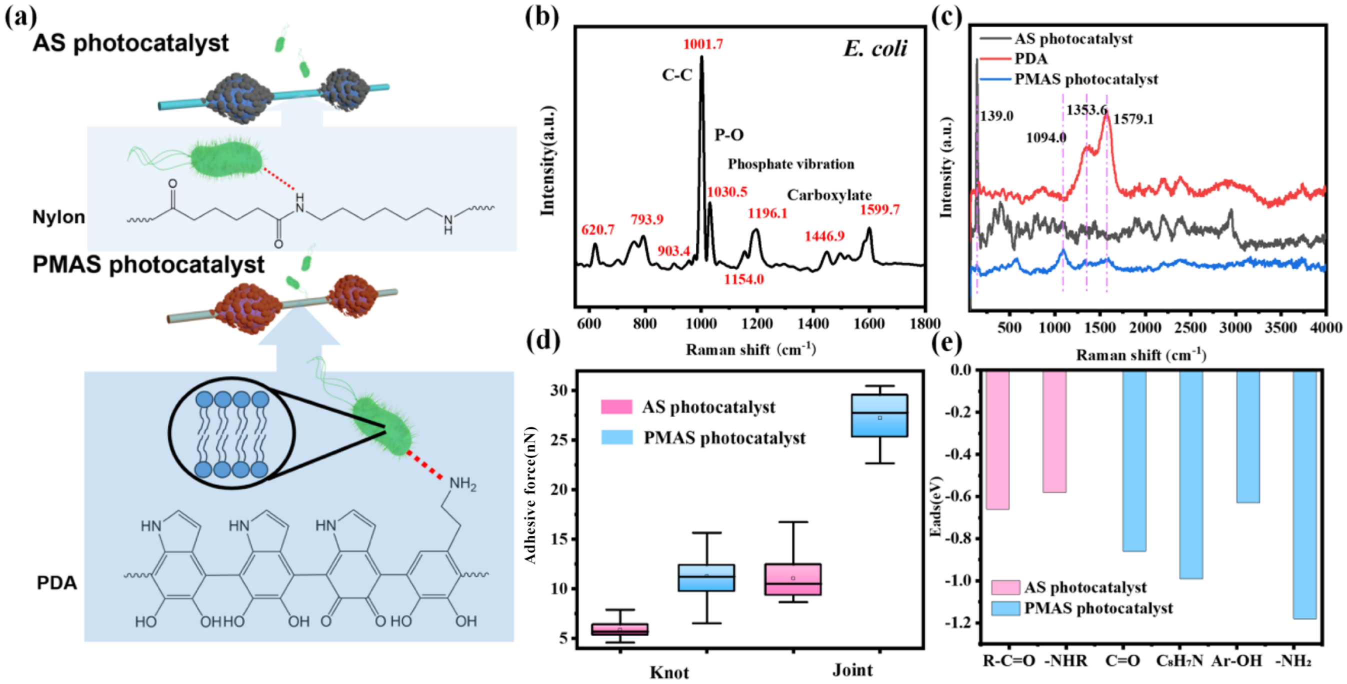

Figure 3. Enhanced airborne bacteria capture mechanisms of PMAS photocatalyst. (a) Illustrations of airborne bacteria absorbed onto functional groups of AS and PMAS photocatalysts; Raman spectra of (b) *E. coli.* and (c) photocatalysts; (d) Statistical adhesive forces of the photocatalysts; (e) Theoretical calculations of interaction energy between microorganisms and functional groups on AS and PMAS photocatalysts.

different concentrations of dopamine hydrochloride (Figure S10), PDA formed a uniform and complete thin film on the photocatalyst at a concentration of 0.5 g/L. The dopamine molecules adsorbed onto the surface of the artificial spider silk photocatalyst, and then the molecules were oxidatively coupled and post-cyclized, forming an adhesive PDA thin film.[41] At a low concentration of dopamine hydrochloride, the film was not complete, while at a high concentration of 1.0 g/L, PDA formed a thick layer, leading to film cracking, particle aggregation, and active site shielding, which reduced bioaerosol capture performance. It can be seen from Figure 2e that the capture performance of the PMAS photocatalyst increased as the treatment time was prolonged from 3 to 24 h, due to the PDA thin film fully forming on the PMAS photocatalyst after 24 h. Although introducing more air into the system and accelerating PDA formation within a short time by stirring, it may also cause structural damage to the PMAS photocatalyst. Therefore, proper PDA modification parameters were also found to significantly enhance the bioaerosol capture efficiency of the PMAS photocatalyst, underscoring the critical role of this modification in improving performance.

To further prove that airborne bacteria were indeed captured by the PMAS photocatalyst, the PMAS photocatalyst, after capturing bioaerosols, was placed on nutrient agar for 18 h of cultivation. The optical image of the PMAS photocatalyst (Figure 2f) shows bacterial colonies observed along the surface of the photocatalyst, indicating the successful capture of airborne bacteria onto it. SEM images (Figure 2g and h) reveal that the surface of the spindle knot of the PMAS photocatalyst was fully covered by bacteria after capturing. In the high magnification image, bacteria were found aggregated together on the spindle knot, while only very few bacteria settled on the joint of the PMAS photocatalyst, indicating that PDA modification may also increase the concentration capability of the PMAS photocatalyst. More bacteria on the spindle knot of the PMAS photocatalyst can be seen compared to the AS photocatalyst, which is consistent with the results of Figure 2a−c. All the above results provide evidence that bioaerosols were captured and concentrated on the spindle knots by the PMAS photocatalyst, and PDA indeed enhances the capture performance of the PMAS photocatalyst.

3.2. Enhanced Capture Mechanism of the PMAS Photocatalyst for Bioaerosols

In a humid environment, bioaerosols contain airborne bacteria and their droplets. Therefore, two representative interfaces, including microorganism photocatalyst and water-photocatalyst, were investigated to reveal the underlying mechanism of the bioaerosol capture performance of the PMAS photocatalyst. For the first interface of microorganism photocatalyst, as PDA modification endowed the PMAS photocatalyst with higher performance for bioaerosol capture, we hypothesized that the origin of these results may come from additional interaction forces provided by PDA modification onto the photocatalyst. As illustrated in Figure 3a, microorganisms in bioaerosols can be captured by the PMAS photocatalyst with various functional groups. The initial interactions between airborne bacteria and photocatalysts were microorganism (cell membrane)−PDA interfaces for PMAS photocatalysts. To confirm if enhanced adsorption forces come from the amino group or indole ring in PDA, experimental and theoretical calculations were both conducted. First, a microscopic confocal Raman spectrometer was applied to investigate the surface chemical composition of *E. coli* (Figure 3b). Phospholipids are the main components of the cell membrane (consistent with literature at 1196.1 cm^{-1}),[47] which were used as representative compositions for the cell membrane. In the meantime, the surface chemical composition of PMAS photocatalysts was also characterized by Raman spectra (Figure 3c). The characteristic peak at 139.0 cm^{-1} is attributed to TiO_2, which can be found in both PMAS and AS photocatalysts (black and blue lines).

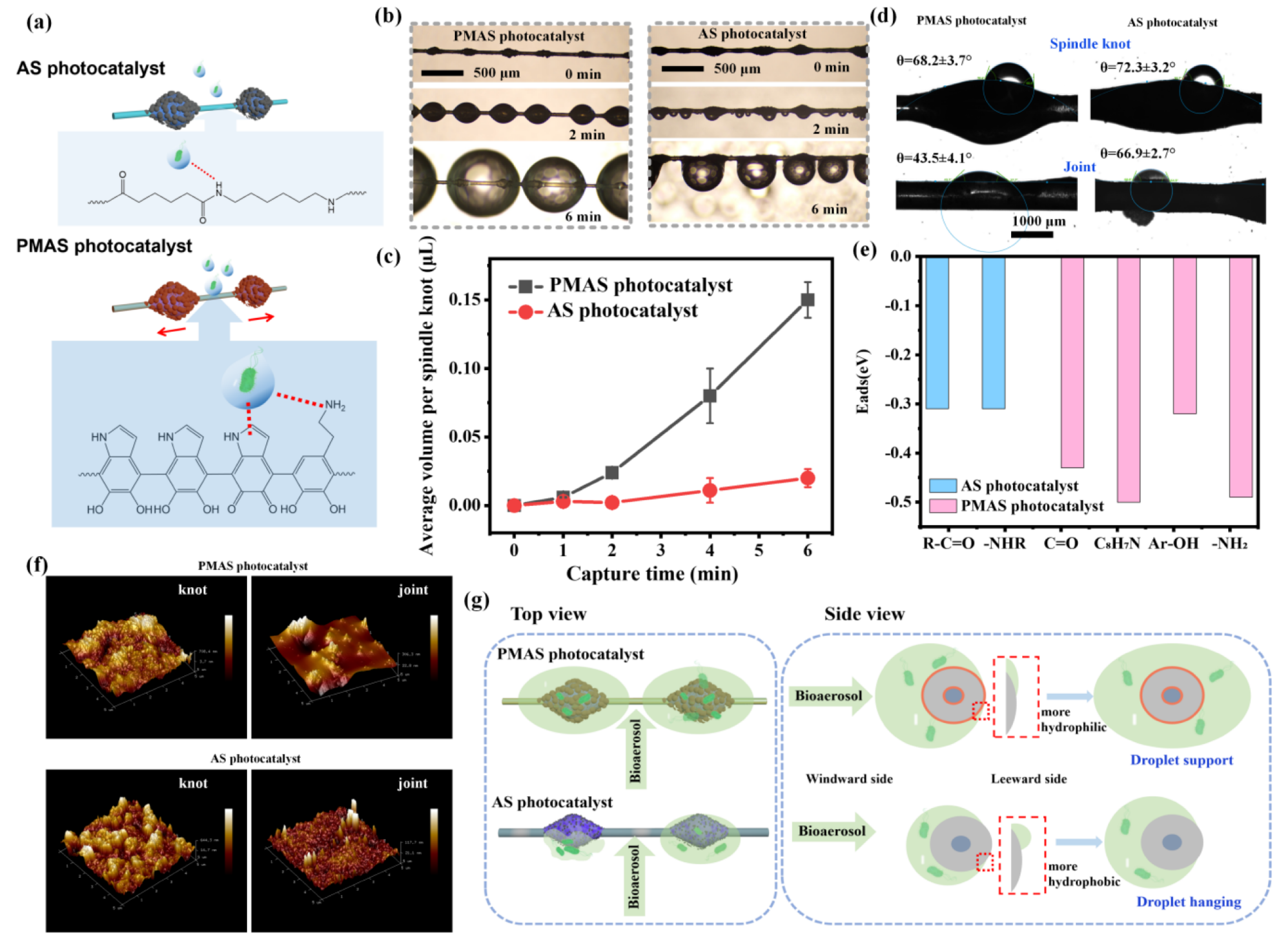

Figure 4. Bacterial droplet capture mechanisms of PMAS photocatalysts. (a) Illustrations of bacterial droplets absorbed onto functional groups of AS and PMAS photocatalysts; (b) Optical images of bacterial droplets captured onto the AS and PMAS photocatalysts under different procedures; (c) The average volume of droplets captured by photocatalysts per spindle knot; (d) Water contact angles of the spindle knot and the joint; (e) Theoretical calculations of interaction energy between droplets and functional groups on AS and PMAS photocatalyst; (f) Surface topography of the spindle knots and the joints; (g) Illustrations of bacterial droplets captured by the photocatalysts from the joint structure, forming microdroplets on the spindle knots.

The characteristic peak at 1579.1 cm^{-1} of the PMAS photocatalyst becomes broadened compared to pure PDA (two strong characteristic peaks at 1353.6 and 1579.1 cm^{-1}), which is ascribed to plane vibration of sp^2 carbon atoms.[34] A peak at 1094.0 cm^{-1} in the PMAS photocatalyst may be attributable to indole ring vibrations of PDA.[34] The PDA with type I or II structure with indole rings was hypothesized to modify the surface of the PMAS photocatalyst (Figure 1b).[48,49] The results indicate the successful modification of PDA with abundant indole ring structures onto the PMAS photocatalyst was observed (although difficult to distinguish in FTIR spectra in Figure S11).

To investigate the actual interaction forces between bioaerosols and the photocatalyst, AFM was applied to detect the adhesive forces between bacteria and the PMAS photocatalyst (Figure 3d). For the PMAS photocatalyst, the adhesive force of the joint (27 nN) is ~2 times higher than that of the spindle knot (12 nN), which provides evidence that the bacteria show stronger affinity to the joints than to the spindle knots. Meanwhile, the adhesive forces for the joint of the AS photocatalyst and the spindle knot are only 10 and 5 nN, respectively, indicating that the interaction between microorganisms and the photocatalyst was enhanced twofold after PDA modification (representative adhesive force curves are shown in Figure S12). These experimental results provide strong evidence that PDA modification enhances the bioaffinity of the PMAS photocatalyst to airborne bacteria.

To further provide insights into the mechanism by which PDA enhances the airborne bacteria capture performance of the PMAS photocatalyst, the interaction between bioaerosols and the PMAS photocatalyst was simulated using DFT. As the dopamine molecule is attached onto TiO_2 surface almost in parallel (Figures S13 and S14) via a π-π bond, no new chemical bond is formed in the PMAS photocatalyst. To calculate the adsorption energy at the interface between airborne bacteria and PMAS photocatalysts (bacteria−PDA interface), the functional groups of indole rings, amine groups, and hydroxyl groups were all chosen as representative groups (Figure 3a top for AS and bottom for the PMAS photocatalyst). For airborne bacteria, the hydrophilic phosphoric acid faces outward from the cell, thus, phosphoric acid was simply used to represent the surface of the bacteria. The calculation results are presented in Figure 3e. For the microorganism and PDA interface (PMAS photocatalyst), the adsorption energy of C═O, C_8H_7N (indole ring), Ar−OH, and $-NH_2$ is obtained as −0.86, −0.99, −0.63, and −1.18

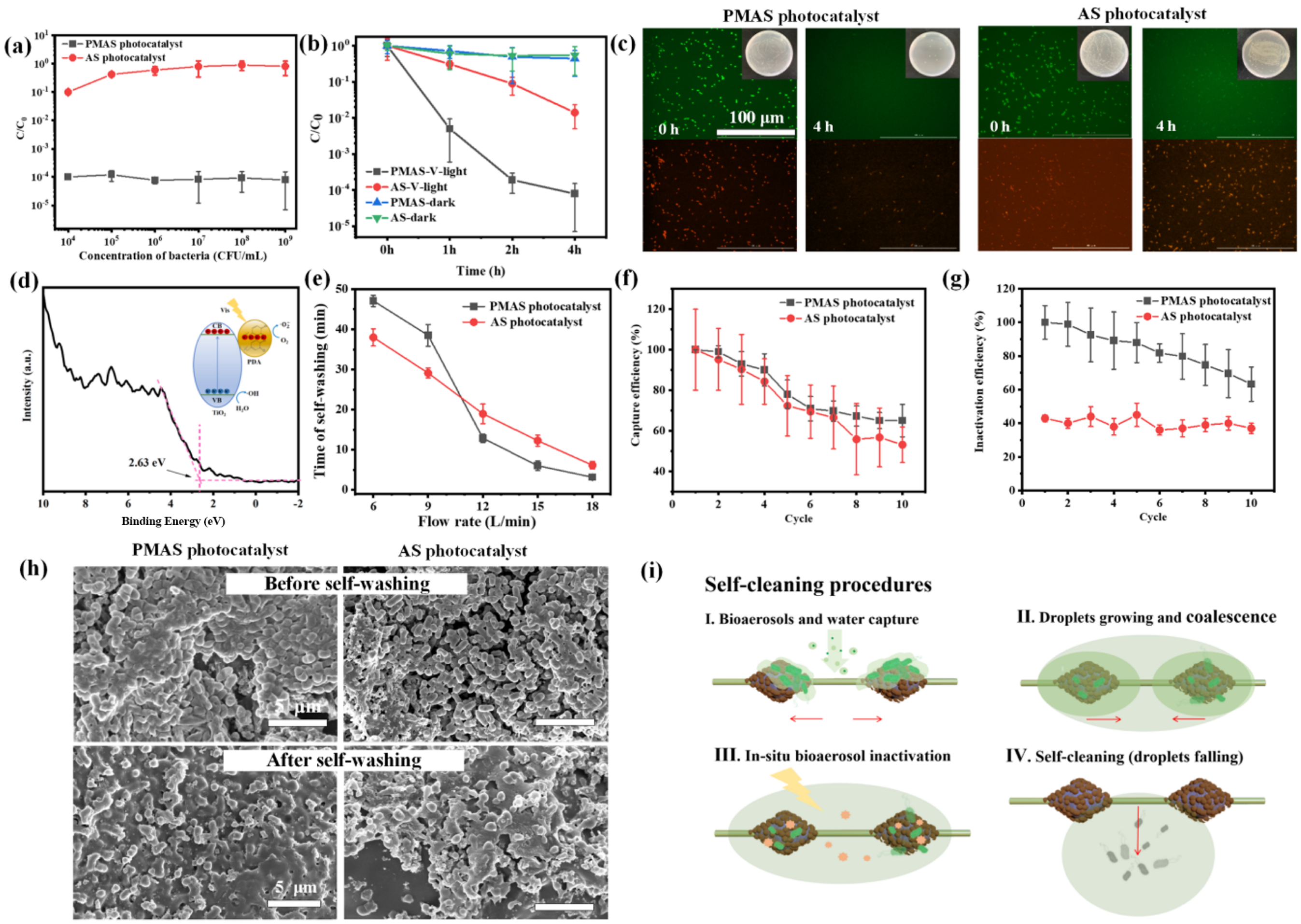

Figure 5. Self-cleaning performance of PMAS photocatalyst. Bioaerosol inactivation performance of photocatalysts at different (a) concentrations of bacteria and (b) irradiation time; (c) Fluorescent images of bacteria in the droplets captured by photocatalysts before and after visible light irradiation; (d) Illustration of electron transfer and valence band of the PMAS photocatalyst; (e) Average self-washing time at different flow rates; (f) Capture and (g) inactivation efficiency of bioaerosols by AS/PMAS photocatalysts after multiple cycles; (h) SEM images of bacteria on spindle knots of AS/PMAS photocatalysts before and after self-washing; (i) Self-cleaning procedures of the PMAS photocatalyst.

eV, respectively, which is twice as high as at the microorganism−nylon (AS photocatalyst) interface, where the adsorption energies of R—C═O and −NHR groups to phosphoric acid are around −0.66 and −0.58 eV, respectively. These results are highly consistent with the experimental results of adhesive forces (Figure 3d). The indole ring and amine groups in PDA indeed offer strong interaction between the surface of the PMAS photocatalyst and the surface phosphoric acid of captured airborne bacteria.

On the other hand, for the second water−photocatalyst interface, as shown in Figure 4a, the surface of some airborne bacteria was wrapped with water; thus, the actual interface was the water−photocatalyst interface during bioaerosol capture in a humid environment. The optical images of the PMAS photocatalyst before and after capturing bioaerosols are shown in Figure 4b. The bioaerosol capture process mainly originates from the joints of the PMAS photocatalyst, and then the small bacterial microdroplets were driven to spindle knots by Laplace pressure and surface tension. The bacterial microdroplets were concentrated into large droplets hanging onto the spindle knots after 2 min and grew even larger, hanging across two spindle knots after 6 min, while for the AS photocatalyst, bacterial microdroplets remained much smaller at the same time. From Figure 4c, the average volume of the microbial droplets per spindle knot of the PMAS photocatalyst was 0.15 μL after 6 min of capture, showing better bacterial droplet capture performance (around 7 times) than the AS photocatalyst (0.02 μL). The hydrophilicity of the PMAS photocatalyst was characterized by the water contact angle, as shown in Figure 4d. The contact angle was measured as 68.2° ± 3.7° and 43.5° ± 4.1° for spindle knots and joints, respectively, which decreased by approximately 20° for the joint and approximately 4° for the spindle knot compared with the AS photocatalyst. This result indicates that the PMAS photocatalyst has the advantages of water collection capability, facilitating bioaerosol (airborne bacteria wrapped with a water film) capture due to its hydrophilic nature.

As presented in Figure 4e, DFT simulation was also conducted to reveal the interaction between bacterial droplets and PMAS photocatalysts (H_2O−PDA interface). For the PMAS photocatalyst, the adsorption energy of PDA to H_2O is −0.43, −0.50, −0.32, and −0.49 eV for C═O, C_8H_7N (indole ring), Ar−OH, and $-NH_2$, respectively, while for the AS photocatalyst (H_2O−nylon interface), nylon to H_2O is only −0.31 and −0.31 eV for R—C═O and −NHR groups (AS photocatalyst), respectively. The indole and amino groups in PDA can offer hydrophilic surfaces onto the PMAS photocatalyst,[50,51] resulting in a strong interaction between its surface and bacterial droplets, forming hydrogen bonds to capture more bacterial droplets (airborne bacteria wrapped with a water film). As the adsorption energy of PDA−bacteria is stronger than that of PDA−H_2O and some of the bacteria are wrapped with a water film at high RH conditions, it is supposed that H_2O adsorption does not significantly influence the capture performance of the PMAS photocatalyst. In addition, liquid droplets can be concentrated on the spindle knots by Laplace pressure, thus exposing and regenerating active sites on the joints.

Although the roughness difference of the PMAS photocatalyst decreased by 36.4%, implying a reduced driving force for bacterial droplet transport (Figure 4f), this effect is outweighed by the enhanced hydrophilicity and bioaffinity from PDA. It is worth noting that droplets quickly move to the leeward side, forming large bacterial droplets on the PMAS photocatalyst, and the droplets fully cover the spindle knots (both windward and leeward sides) and exhibit larger volume, whereas droplets only half-wrap the knots for the AS photocatalyst (windward side only), as shown in Figure 4b. A possible explanation is that the bacterial droplets initially interacted with the PMAS photocatalyst on the windward side but then rapidly migrated to the leeward side due to the hydrophilicity, bioaffinity, and spindle structure of it (Figure 4g). This process freed up the windward side for subsequent capture, resulting in larger bacterial droplet volumes that were captured and supported on the PMAS photocatalyst. Thus, PDA modification enhances the bioaerosol capture performance of the PMAS photocatalyst by improving the interaction between the interface of water and photocatalyst.

3.3. Enhanced Purification and Self-Cleaning Mechanism of the PMAS Photocatalyst

The enhanced purification performance of the PMAS photocatalyst under visible light was evaluated by its bacterial inactivation efficiency. First, the bacterial inactivation performance of the PMAS photocatalyst with different concentrations of bioaerosols is shown in Figure 5a. Under visible light, 99.99% of the captured bioaerosols were inactivated by the PMAS photocatalyst. With prolonged irradiation time, the number of living bacteria captured by the PMAS photocatalyst declined remarkably (Figure 5b and c) as compared with the AS photocatalyst. The results show that the PDA modification truly enhanced the photocatalytic properties of the PMAS photocatalyst under visible light, as the AS photocatalyst could not inactivate bioaerosols due to the inability of TiO_2 to harvest visible light. These results confirm that the PMAS photocatalyst possesses superior photocatalytic inactivation performance under visible light, which may be safer for practical applications compared to using UV light.

As shown in Figure 5d inset, PDA acts as a photosensitizer, absorbing visible light and injecting excited electrons into the conduction band of TiO_2 (This interfacial electron transfer achieves effective charge separation, allowing TiO_2 to utilize visible light for photocatalytic reactions while the holes remain in the PDA layer.) This process produces ROSs (Figure S15), thereby endowing the PMAS photocatalyst with photocatalytic properties under visible light. As the captured bioaerosol is concentrated in liquid droplets by the PMAS photocatalyst, the ROSs ($^{\bullet}$OH and H_2O_2) produced in this liquid photocatalytic system can diffuse within the droplet for further inactivation processes without direct contact,[52] facilitating the damage to cells, proteins, DNA, and other components, breaking them down into debris.[53] The leaked intracellular substances and cell debris can be further degraded and ultimately mineralized through prolonged photocatalytic treatment, provided the process is sufficiently long,[54] allowing them to be completely dissolved in water.[55] Therefore, PDA extends the photoresponse range of the PMAS photocatalyst, endowing it with photocatalytic performance under visible light to inactivate and further mineralize captured bioaerosols, resulting in enhanced purification performance of the PMAS photocatalyst.

The enhanced self-washing performance of the PMAS photocatalyst was also evaluated by measuring the time required for the first bacterial droplet (cell debris) to be removed by gravity at different flow rates (Figure 5e). At low flow rates (6 and 9 L/min), the PMAS photocatalyst exhibited a long self-washing time of around 46 min, but only around 5 min at high flow rates (≥12 L/min) due to the enhanced bioaerosol and water collection capability of the PMAS photocatalyst. This phenomenon can be explained by the fact that the PMAS photocatalyst can support larger bacterial droplet volumes before being removed by gravity at low flow rates, resulting in a longer self-washing time, which is up to 7 times greater than that of the AS photocatalyst (Figure 4c). The capability of the PMAS photocatalyst to capture large volumes of bacterial liquid facilitates its application in practical situations with relatively lower humidity levels than laboratory conditions, as water is necessary in the photocatalytic process to form $^{\bullet}$OH radicals, and a large volume of water is beneficial to the self-washing process. At high flow rates, the PMAS photocatalyst captures bacterial droplets efficiently (Figure 2c) to reach its maximum bacterial capture, and then the bacterial droplets are quickly removed by gravity to expose more capture sites to bioaerosols. These results confirmed that the PDA modification can also enhance the self-washing capability of the PMAS photocatalyst for bioaerosol purification through gravity removal at different flow rates.

The self-cleaning property of the PMAS photocatalyst was achieved through a combination of photocatalytic inactivation and the self-washing of cell debris by gravity. Figure 5f and g shows the bioaerosol capture and inactivation performance of the PMAS photocatalyst over multiple self-washing cycles. After 10 cycles, the capture and inactivation efficiencies of the PMAS photocatalyst decreased slightly from 100% to about 65% and from 99% to 60%, respectively, which were still much higher than those of the AS photocatalyst, which sustained an inherently low efficiency. SEM images (Figure 5h) and element mapping (Figure S16) confirmed that very few bacterial debris remained on the PMAS photocatalyst after self-washing, demonstrating that the bioaerosol inactivated on the PMAS photocatalyst was indeed self-washed by gravity.

Therefore, the self-cleaning property of the PMAS photocatalyst consists of *in situ* bacterial inactivation and continuous self-washing, thus enabling photocatalyst regeneration. As illustrated in Figure 5i, the self-cleaning process of the PMAS photocatalyst is summarized in four key steps: I: Microorganisms and microdroplets in bioaerosols are captured and directionally concentrated onto the spindle knots, forming microreactors; II: Over time, the droplets grow and merge into larger droplets spanning multiple knots; III: Under visible light irradiation, ROSs are generated and diffuse within the droplets, inactivating and mineralizing the trapped microorganisms; IV: Once inactivated and mineralized, the biodebris is washed away by the falling droplet under gravity without residues adhering to the surface, and then the PMAS photocatalyst achieves self-cleaning and regeneration of the reactive sites of the PMAS photocatalyst.

The PDA modification enhances microorganism and bacterial droplet capture and photocatalytic inactivation performance of the PMAS photocatalyst, resulting in an effective self-cleaning property. This allows the PMAS photocatalyst to be reused for bioaerosol purification under high humidity and high airflow conditions, which realizes a highly efficient and long-term bioaerosol control strategy.

3.4. Environmental Implications

Bioaerosols represent a growing public health concern, capable of spreading infectious diseases and posing risks to human health. Conventional bioaerosol control technology often fails under high-humidity conditions due to the loss of electrostatic adsorption and lack of antimicrobial activity, leading to issues such as low efficiency, pore blockage, limited service time, and secondary contamination. To address these challenges, a bioinspired PMAS photocatalyst capable of highly efficient capture, inactivation, and self-cleaning in high-humidity environments was developed. Unlike conventional air filters that rely solely on physical interception, the PMAS photocatalyst utilizes bioadhesion and photocatalytic inactivation, enabled by its PDA-modified artificial spider silk structure. This PMAS photocatalyst enhances microorganism and microbial droplet capture, *in situ* inactivation, and self-cleaning through strong interfacial interactions between bioaerosols and the photocatalyst offered by PDA modification. These results indicate that tailoring the design of material structures and bioinspired surface modifications to enhance a high affinity to both microorganisms and their liquid droplets is a helpful photocatalytic strategy for bioaerosol control. This strategy offers a foundational solution to mitigate bioaerosol threats, and it is of strategic significance to the prevention and control of bioaerosol epidemics. In addition, our findings provide fundamental insight into the mechanism of surface modification-enhanced capture, photocatalytic inactivation, as well as the regeneration of reactive sites, which establishes a new design principle for enhancing interfacial interactions for more efficient and adaptive bioaerosol control technologies. While the properties of PDA modification suggest efficient capture performance and promising durability, future work should focus on long-term field trials to systematically evaluate the coating's lifespan, possible performance decrease, and any secondary environmental impacts under realistic environmental conditions. Such investigations would be crucial to bridge the gap between laboratory research and practical implementation. Future development of bioaerosol control technologies should incorporate material functionalization to achieve sustainable air purification for long-term use.

ASSOCIATED CONTENT

Supporting Information

The Supporting Information is available free of charge at https://pubs.acs.org/doi/10.1021/acsestengg.6c00164.

> Additional information on preparation procedures, experimental setups; figures of morphology, element mappings, chemical compositions, and ROS generation of PMAS photocatalyst; size distribution of bioaerosols; simulations of dopamine adsorption and interaction between PDA and bioaerosols (PDF)

AUTHOR INFORMATION

Corresponding Author

Taicheng An — *Guangdong Key Laboratory of Environmental Catalysis and Health Risk Control, Guangdong-Hong Kong-Macao Joint Laboratory for Contaminants Exposure and Health, Institute of Environmental Health and Pollution Control, Guangdong University of Technology, Guangzhou 510006, China; Guangdong Engineering Technology Research Center for Photocatalytic Technology Integration and Equipment, Guangdong Basic Research Center of Excellence for Ecological Security and Green Development, School of Environmental Science and Engineering, Guangdong University of Technology, Guangzhou 510006, China;* orcid.org/0000-0001-6918-8070;
Email: antc99@gdut.edu.cn

Authors

Linghui Peng — *Guangdong Key Laboratory of Environmental Catalysis and Health Risk Control, Guangdong-Hong Kong-Macao Joint Laboratory for Contaminants Exposure and Health, Institute of Environmental Health and Pollution Control, Guangdong University of Technology, Guangzhou 510006, China; Guangdong Engineering Technology Research Center for Photocatalytic Technology Integration and Equipment, Guangdong Basic Research Center of Excellence for Ecological Security and Green Development, School of Environmental Science and Engineering, Guangdong University of Technology, Guangzhou 510006, China*

Weina Zhao — *Guangdong Key Laboratory of Environmental Catalysis and Health Risk Control, Guangdong-Hong Kong-Macao Joint Laboratory for Contaminants Exposure and Health, Institute of Environmental Health and Pollution Control, Guangdong University of Technology, Guangzhou 510006, China*

Fukai Xu — *Guangdong Key Laboratory of Environmental Catalysis and Health Risk Control, Guangdong-Hong Kong-Macao Joint Laboratory for Contaminants Exposure and Health, Institute of Environmental Health and Pollution Control, Guangdong University of Technology, Guangzhou 510006, China*

Manlin Dong — *Guangdong Key Laboratory of Environmental Catalysis and Health Risk Control, Guangdong-Hong Kong-Macao Joint Laboratory for Contaminants Exposure and Health, Institute of Environmental Health and Pollution Control, Guangdong University of Technology, Guangzhou 510006, China*

Guiying Li — *Guangdong Key Laboratory of Environmental Catalysis and Health Risk Control, Guangdong-Hong Kong-Macao Joint Laboratory for Contaminants Exposure and Health, Institute of Environmental Health and Pollution Control, Guangdong University of Technology, Guangzhou 510006, China; Guangdong Engineering Technology Research Center for Photocatalytic Technology Integration and Equipment, Guangdong Basic Research Center of Excellence for Ecological Security and Green Development, School of Environmental Science and Engineering, Guangdong University of Technology, Guangzhou 510006, China;* orcid.org/0000-0002-6777-4786

Weiping Zhang — *Guangdong Key Laboratory of Environmental Catalysis and Health Risk Control, Guangdong-Hong Kong-Macao Joint Laboratory for*

Contaminants Exposure and Health, Institute of Environmental Health and Pollution Control, Guangdong University of Technology, Guangzhou 510006, China

Zhishu Liang – *Guangdong Key Laboratory of Environmental Catalysis and Health Risk Control, Guangdong-Hong Kong-Macao Joint Laboratory for Contaminants Exposure and Health, Institute of Environmental Health and Pollution Control, Guangdong University of Technology, Guangzhou 510006, China;* orcid.org/0009-0006-2048-514X

Huijun Zhao – *Guangdong Key Laboratory of Environmental Catalysis and Health Risk Control, Guangdong-Hong Kong-Macao Joint Laboratory for Contaminants Exposure and Health, Institute of Environmental Health and Pollution Control, Guangdong University of Technology, Guangzhou 510006, China; Guangdong Engineering Technology Research Center for Photocatalytic Technology Integration and Equipment, Guangdong Basic Research Center of Excellence for Ecological Security and Green Development, School of Environmental Science and Engineering, Guangdong University of Technology, Guangzhou 510006, China;* orcid.org/0000-0002-3028-0459

Complete contact information is available at: https://pubs.acs.org/10.1021/acsestengg.6c00164

Notes

The authors declare no competing financial interest.

■ ACKNOWLEDGMENTS

This work was supported by the National Key Research and Development Program of China (2023YFC3708204), NSFC (42207112), the Introduction of Innovative and Research Teams Project of the Guangdong Pearl River Talents Program (2023ZT10L102), and the Science and Technology Project of Guangdong Province, China (2025A1515011295).

■ REFERENCES

(1) Tang, J. W.; Marr, L. C.; Li, Y.; Dancer, S. J. Covid-19 has redefined airborne transmission. *BMJ* **2021**, *373*, n913.

(2) Wang, C. C.; Prather, K. A.; Sznitman, J.; Jimenez, J. L.; Lakdawala, S. S.; Tufekci, Z.; Marr, L. C. Airborne transmission of respiratory viruses. *Science* **2021**, *373* (6558), No. eabd9149.

(3) Xie, W.; Li, Y.; Bai, W.; Hou, J.; Ma, T.; Zeng, X.; Zhang, L.; An, T. The source and transport of bioaerosols in the air: A review. *Front. Environ. Sci. Eng.* **2021**, *15* (3), 44.

(4) Amin, H.; Santl-Temkiv, T.; Cramer, C.; Finster, K.; Real, F. G.; Gislason, T.; Holm, M.; Janson, C.; Jogi, N. O.; Jogi, R.; Malinovschi, A.; Marshall, I. P. G.; Modig, L.; Norback, D.; Shigdel, R.; Sigsgaard, T.; Svanes, C.; Thorarinsdottir, H.; Wouters, I. M.; Schlunssen, V.; Bertelsen, R. J. Indoor airborne microbiome and endotoxin: Meteorological events and occupant characteristics are important determinants. *Environ. Sci. Technol.* **2023**, *57* (32), 11750–11766.

(5) Peng, L.; Peng, C.; Li, G.; An, T. A critical mini-review on atmospheric ozone mediated alterations of bioaerosols and their effects on human health. *Global Environ. Sci.* **2025**, *1* (1), 35–42.

(6) Nielsen, L. S.; Santl-Temkiv, T.; Palomeque Sanchez, M.; Massling, A.; Ward, J. C.; Jensen, P. B.; Boesen, T.; Petters, M.; Finster, K.; Bilde, M.; Rosati, B. Water uptake of airborne cells of *P. syringae* measured with a hygroscopicity tandem differential mobility analyzer. *Environ. Sci. Technol.* **2024**, *58* (43), 19211–19221.

(7) Zhang, Z.; Li, J.; Jiang, Y.; Zhao, L.; Bai, L.; Yang, J.; Pang, H.; Lu, J. Emission characteristics of aerosols generated during the micro-nano bubble aeration process in wastewater. *Environ. Sci. Technol.* **2024**, *58* (39), 17396–17405.

(8) Quon, H.; Ram, D.; Sylvestre, É.; Hamilton, K. A. The role of aspiration in legionnaires' disease: A quantitative microbial risk assessment (QMRA)-based comparison with inhalation exposures. *Environ. Sci. Technol. Lett.* **2025**, *12* (7), 785–791.

(9) Yan, S.; Liu, Q.; Wen, Z.; Liang, B.; Liu, Z.; Xing, J.; Li, J.; Zhang, M.; Liu, X.; Wang, C.; Xing, D. An AIE-active Janus filter membrane for highly efficient detection and elimination of bioaerosols. *J. Hazard. Mater.* **2025**, *492*, 138116.

(10) Chung, M. W.; Choi, M.; Lee, B.; He, F.; Kim, J. H.; Weon, S. Carbon cocatalysts self-destruction in photocatalytic air purification. *Environ. Sci. Technol.* **2025**, *59* (24), 12314–12327.

(11) Zhang, R.; Liu, C.; Hsu, P. C.; Zhang, C.; Liu, N.; Zhang, J.; Lee, H. R.; Lu, Y.; Qiu, Y.; Chu, S.; Cui, Y. Nanofiber air filters with high-temperature stability for efficient PM2.5 removal from the pollution sources. *Nano Lett.* **2016**, *16* (6), 3642–3649.

(12) Lu, S.; Meng, G.; Wang, C.; Chen, H. Photocatalytic inactivation of airborne bacteria in a polyurethane foam reactor loaded with a hybrid of MXene and anatase TiO_2 exposing 001 facets. *Chem. Eng. J.* **2021**, *404*, 126526.

(13) Shen, H.; Zhou, Z.; Wang, H.; Zhang, M.; Han, M.; Durkin, D. P.; Shuai, D.; Shen, Y. Development of electrospun nanofibrous filters for controlling coronavirus aerosols. *Environ. Sci. Technol. Lett.* **2021**, *8* (7), 545–550.

(14) Si, Y.; Zhang, Z.; Wu, W.; Fu, Q.; Huang, K.; Nitin, N.; Ding, B.; Sun, G. Daylight-driven rechargeable antibacterial and antiviral nanofibrous membranes for bioprotective applications. *Sci. Adv.* **2018**, *4* (3), No. eaar5931.

(15) Singh, S.; Vishwakarma, P.; Gupta, T. Review of current and future indoor air purifying technologies. *ACS ES&T Eng.* **2024**, *4* (11), 2607–2630.

(16) Li, P.; Li, J.; Feng, X.; Li, J.; Hao, Y.; Zhang, J.; Wang, H.; Yin, A.; Zhou, J.; Ma, X.; et al. Metal-organic frameworks with photocatalytic bactericidal activity for integrated air cleaning. *Nat. Commun.* **2019**, *10* (1), 2177.

(17) Fischer, E. P.; Fischer, M. C.; Grass, D.; Henrion, I.; Warren, W. S.; Westman, E. Low-cost measurement of face mask efficacy for filtering expelled droplets during speech. *Sci. Adv.* **2020**, *6* (36), No. eabd3083.

(18) Jin, L.; Chen, M.; Chen, Z.; Li, M.; Yao, M.; Lu, Y. Efficient air disinfection achieved by nanowire-modified copper mesh electrodes. *ACS ES&T Eng.* **2024**, *4* (6), 1422–1432.

(19) Getnet, M. E.; Dlamini, W. N.; Liao, C.-H.; Berekute, A. K.; Chen, A.-F.; Sallah-Ud-Din, R.; Siregar, S.; Wu, Y.-C.; Shen, W.-T.; Bai, C.-H.; et al. Improving hospital air quality with a nano-Ag/chitosan-TiO_2 filter system and cloud-based monitoring. *Indoor Air* **2025**, *2025* (1), 8243815.

(20) Yong, S. -S.; Jyung, S.; Kim, D. -K.; Kim, S. -H.; Kang, D. -H. Photocatalytic ZnO-doped polyester filters for reducing airborne cross-contamination by foodborne pathogens in storage environments. *Food Res. Int.* **2025**, *221* (Pt 4), 117628.

(21) Kalani, S.; Islam, M. S.; Li, J.; Rawlins, J.; Ward, V. C. A.; Mekonnen, T. H. Scalable antimicrobial air filters: Polypropylene/rose bengal melt-blown nonwoven filters. *Chemosphere* **2025**, *384*, 144514.

(22) Liu, L.; Shen, Z.; Wang, C. Highly efficient visible-light-driven photocatalytic disinfection of flowing bioaerosol using mono/multilayer MXene based catalyst. *Chem. Eng. J.* **2023**, *457*, 141327.

(23) Li, Y.; Shen, R.; He, W.; Luo, Q.; Zhou, X.; Yang, J.; Liu, J. Plastic optical fiber-driven distributed photocatalysis in NWP-PDA-RGO-TiO_2 filter for simultaneous formaldehyde degradation, particulate removal and bioaerosol inactivation. *Chem. Eng. J.* **2025**, *523*, 168508.

(24) Liu, L.; Shen, Z.; Wang, C. Accelerating photocatalytic bioaerosol disinfection at catalyst-cell interface via monolayer $Ti_3C_2T_x$ introduction. *Sci. Bull.* **2025**, *70* (6), 832–836.

(25) Peng, L.; Wang, H.; Li, G.; Liang, Z.; Zhang, W.; Zhao, W.; An, T. Bioinspired artificial spider silk photocatalyst for the high-efficiency capture and inactivation of bacteria aerosols. *Nat. Commun.* **2023**, *14* (1), 2412.

(26) Anandan, S.; Fix, A. J.; Freeman, A. J.; Miller, L.; Scheg, D. P.; Morgan, X.; Park, J. H.; Horton, W. T.; Blatchley, E. R.; Warsinger, D.

M. Framework for assessing collection-based photocatalytic oxidation systems in HVAC applications for bioaerosol control. *Build. Environ.* **2024**, *261*, 111593.

(27) Heo, K. J.; Lim, C. E.; Kim, H. B.; Lee, B. U. Effects of human activities on concentrations of culturable bioaerosols in indoor air environments. *J. Aerosol Sci.* **2017**, *104*, 58−65.

(28) Qi, J.; Yin, Y.; Zhang, D.; Li, H.; Dong, L. The concentration, size distribution and dry deposition flux of microbes in atmospheric aerosols over the marginal seas and Northwest Pacific Ocean. *Atmos. Res.* **2022**, *265*, 105906.

(29) Peng, L.; Wang, H.; Wang, Y.; Li, G.; An, T. Photocatalytic inactivation technologies for bioaerosols: Advances and perspective. *EES Catal.* **2024**, *2* (1), 138−156.

(30) Guo, F.; Chen, J.; Zhao, J.; Chen, Z.; Xia, D.; Zhan, Z.; Wang, Q. Z-scheme heterojunction g-C_3N_4@PDA/BiOBr with biomimetic polydopamine as electron transfer mediators for enhanced visible-light driven degradation of sulfamethoxazole. *Chem. Eng. J.* **2020**, *386*, 124014.

(31) Hu, C.; Long, L.; Cao, J.; Zhang, S.; Wang, Y. Dual-crosslinked mussel-inspired smart hydrogels with enhanced antibacterial and angiogenic properties for chronic infected diabetic wound treatment via pH-responsive quick cargo release. *Chem. Eng. J.* **2021**, *411*, 128564.

(32) Mei, Y.; Yu, K.; Yazdani-Ahmadabadi, H.; Lange, D.; Kizhakkedathu, J. N. Hydrophilic polymer-guided polycatecholamine assembly and surface deposition. *ACS Appl. Mater. Interfaces* **2022**, *14* (34), 39577−39590.

(33) Jiang, K.; Li, F.; Zhao, X.; Pan, Y. Eco-friendly dopamine-modified silica nanoparticles for oil-repellent coatings: Implications for underwater self-cleaning and antifogging applications. *ACS Appl. Nano Mater.* **2022**, *5* (6), 8038−8047.

(34) Peng, L.; Wang, H.; Li, G.; Zhang, W.; Liang, Z.; An, T. Photocatalytic inactivation of airborne bacteria onto g-C_3N_4/TiO_2/Ni-polydopamine/Ni bifunctional coupling filter with non-size dependent capture effect. *Appl. Catal., B* **2023**, *329*, 122580.

(35) Wu, Y.; Niu, J.; Yuan, X.; Liu, Y.; Zhai, S.; Zhao, Y. Polydopamine and calcium functionalized fiber carrier for enhancing microbial attachment and Cr(VI) resistance. *Sci. Total Environ.* **2023**, *903*, 166626.

(36) Huo, Z.-Y.; Liu, H.; Wang, W.-L.; Wang, Y.-H.; Wu, Y.-H.; Xie, X.; Hu, H.-Y. Low-voltage alternating current powered polydopamine-protected copper phosphide nanowire for electroporation-disinfection in water. *J. Mater. Chem. A* **2019**, *7* (13), 7347−7354.

(37) Cheng, W.; Zeng, X.; Chen, H.; Li, Z.; Zeng, W.; Mei, L.; Zhao, Y. Versatile polydopamine platforms: Synthesis and promising applications for surface modification and advanced nanomedicine. *ACS Nano* **2019**, *13* (8), 8537−8565.

(38) Shen, H.; Long, Y.; Yang, X.; Zhao, N.; Xu, J. Facile fabrication of metal oxide hollow spheres using polydopamine nanoparticles as active templates. *Polym. Int.* **2015**, *64* (8), 986−991.

(39) Zhang, C.; Zhou, Y.; Han, H.; Zheng, H.; Xu, W.; Wang, Z. Dopamine-triggered hydrogels with high transparency, self-adhesion, and thermoresponse as skinlike sensors. *ACS Nano* **2021**, *15* (1), 1785−1794.

(40) Ahn, B. K. Perspectives on mussel-inspired wet adhesion. *J. Am. Chem. Soc.* **2017**, *139* (30), 10166−10171.

(41) Zhang, X.; Lu, B.; Jin, L. N.; Yang, S.; Wang, C.; Tai, J.; Li, D.; Chen, J. Emission dynamics and public health implications of airborne pathogens and antimicrobial resistance from urban waste collection facilities. *Environ. Sci. Technol.* **2025**, *59* (16), 8060−8072.

(42) Rahman, M. A.; Akter, P.; Habib, M. R.; Rahman, M. A.; Mahiuddin, M.; Rahman, M. M.; Islam, M. S.; Miah, M. A. J.; Ahmad, H. Functionalization of biomimetic polydopamine shells constructed onto bismuth-core particles for ph-mediated drug targeting to heal bacterial infections. *Bioconjugate Chem.* **2025**, *36* (3), 563−577.

(43) Li, Y.; Liu, J.; Chen, X.; Yuan, X.; Li, N.; He, W.; Feng, Y. Enhanced electricity generation and extracellular electron transfer by polydopamine−reduced graphene oxide (PDA−rGO) modification for high-performance anode in microbial fuel cell. *Chem. Eng. J.* **2020**, *387*, 123408.

(44) Niu, Z.; Zhao, Y.; Sun, W.; Shi, S.; Gong, Y. Biomimetic surface modification of polypropylene by surface chain transfer reaction based on mussel-inspired adhesion technology and thiol chemistry. *Appl. Surf. Sci.* **2016**, *386*, 41−50.

(45) Zeiri, L.; Bronk, B. V.; Shabtai, Y.; Eichler, J.; Efrima, S. Surface-enhanced raman spectroscopy as a tool for probing specific biochemical components in bacteria. *Appl. Spectrosc.* **2004**, *58* (1), 33−40.

(46) Salazar, P.; Martín, M.; González-Mora, J. L.Polydopamine-modified surfaces in biosensor applications*Polymer Science: Research Advances, Practical Applications and Educational Aspects*Formatex Research Center SL20167385−396

(47) Zhang, L.; Wu, J.; Wang, Y.; Long, Y.; Zhao, N.; Xu, J. Combination of bioinspiration: A general route to superhydrophobic particles. *J. Am. Chem. Soc.* **2012**, *134* (24), 9879−9881.

(48) Ryu, J. H.; Messersmith, P. B.; Lee, H. Polydopamine Surface Chemistry: A Decade of Discovery. *ACS Appl. Mater. Interfaces* **2018**, *10* (9), 7523−7540.

(49) Ke, Q.; Zhang, Y.; Qin, Z.; Meng, Q.; Huang, X.; Kou, X.; Zhang, Y. Polydopamine-functionalized capsules: From design to applications. *J. Controlled Release* **2025**, *378*, 1114−1138.

(50) Gissler, C.; Band, S.; Peer, A.; Ihmsen, M.; Teschner, M. Generalized drag force for particle-based simulations. *Comput. Graph.* **2017**, *69*, 1−11.

(51) Xi, Z.-Y.; Xu, Y.-Y.; Zhu, L.-P.; Wang, Y.; Zhu, B.-K. A facile method of surface modification for hydrophobic polymer membranes based on the adhesive behavior of poly(DOPA) and poly(dopamine). *J. Membr. Sci.* **2009**, *327* (1−2), 244−253.

(52) Shi, H.; Huang, G.; Xia, D.; Ng, T. W.; Yip, H. Y.; Li, G.; An, T.; Zhao, H.; Wong, P. Role of in situ resultant H_2O_2 in the visible-light-driven photocatalytic inactivation of E. coli using natural sphalerite: A genetic study. *J. Phys. Chem. B* **2015**, *119* (7), 3104−3111.

(53) Jiang, Q.; Yin, H.; Li, G.; Liu, H.; An, T.; Wong, P. K.; Zhao, H. Elimination of antibiotic-resistance bacterium and its associated/dissociative bla(TEM-1) and aac(3)-II antibiotic-resistance genes in aqueous system via photoelectrocatalytic process. *Water Res.* **2017**, *125*, 219−226.

(54) Sun, H.; Li, G.; Nie, X.; Shi, H.; Wong, P. K.; Zhao, H.; An, T. Systematic approach to in-depth understanding of photoelectrocatalytic bacterial inactivation mechanisms by tracking the decomposed building blocks. *Environ. Sci. Technol.* **2014**, *48* (16), 9412−9419.

(55) Li, G.; Liu, X.; Zhang, H.; An, T.; Zhang, S.; Carroll, A. R.; Zhao, H. In situ photoelectrocatalytic generation of bactericide for instant inactivation and rapid decomposition of Gram-negative bacteria. *J. Catal.* **2011**, *277* (1), 88−94.